Near field acoustic streaming jet

Brahim Moudjed, Valéry Botton, Daniel Henry, Séverine Millet, Jean-Paul
Garandet, Hamda Ben Hadid

Near field acoustic streaming jet

B. Moudjed[1], V. Botton[1], D. Henry[1], S. Millet[1], J. P. Garandet[2]
and H. Ben Hadid[1]

[1]Laboratoire de Mécanique des Fluides et d'Acoustique, CNRS/Université de Lyon,
École Centrale de Lyon/Université Lyon 1/INSA de Lyon,
ECL, 36 avenue Guy de Collongue, 69134 Ecully Cedex, France
[2]CEA, Laboratoire d'Instrumentation et d'Expérimentation en Mécanique des Fluides et
Thermohydraulique, DEN/DANS/DM2S/STMF/LIEFT, CEA-Saclay, F-91191 Gif-sur-Yvette
Cedex, France

10 septembre 2014

Résumé

A numerical and experimental investigation of the acoustic streaming flow in the near field of
a circular plane ultrasonic transducer in water has been performed. The experimental domain is
a parallelepipedic cavity delimited by absorbing walls to avoid acoustic reflection, with a top free
surface. The flow velocities are measured by PIV, leading to well resolved velocity profiles. The
theoretical model is based on a linear acoustic propagation model, which correctly reproduces the
acoustic field mapped experimentally using a hydrophone, and an acoustic force term introduced
in the Navier Stokes equations under the plane wave assumption. A good agreement between the
experimental measurements and the numerical results for the velocity field is obtained, validating
our numerical approach. The flow structure is found to be correlated with the acoustic field shape.
Indeed, the longitudinal profiles of the velocity present a wavering linked to the variations in acoustic
intensity along the beam axis and transverse profiles exhibit a complex shape strongly influenced
by the transverse variations of the acoustic intensity in the beam. Finally the velocity in the jet is
found to increase as the square root of the acoustic power times the distance from the origin of the
jet over a major part of the cavity.

1   Introduction

The ability of acoustic fields to drive steady flows in fluids has been known for decades [1] and
is usually referred to as acoustic streaming. This phenomenon is, willingly or not, present in a number
of applications ranging from ultrasound-based velocimetry [2, 3] to medical applications [4, 5], from
heat and mass transfer [6, 7, 8, 9, 10] to sonochemistry [11]. It can be seen as a coupling between
acoustic propagation within an otherwise incompressible flow. This coupling is often accounted for
by an additional force term in the Navier-Stokes equations for a viscous incompressible flow. For
a continuous progressive acoustic plane wave propagating along the x direction, this force can be

expressed, at every location, as [12]

$$\vec{f}_{ac} = \frac{2\alpha_{ac}}{c} I_{ac}\vec{x} \, , \tag{1}$$

with I_{ac}, **the temporal average acoustic intensity**, α_{ac}, the acoustic pressure wave attenuation coefficient ($\alpha = 0.1\text{m}^{-1}$) and c, the sound celerity ($c = 1480\text{m.s}^{-1}$). The acoustic field, however, is known to often involve diffraction effects, as shown in our recent experimental investigation in the acoustic far-field [13]. The flow structure was found to be strongly correlated to the shape of the acoustic beam, so that a conclusion was that accounting for diffraction is a key ingredient in the modeling of acoustic streaming.

A few years ago, Kamakura *et al.* (1996) performed an experimental and theoretical study of acoustic streaming in the near field of a plane transducer. Their theoretical approach relies on a physically intricate non-linear propagation model including diffraction, attenuation and nonlinear effects to compute the acoustic streaming force field. They solve the so-called KZK equation [14, 15] with appropriate boundary conditions for the acoustic pressure. From the obtained acoustic pressure field, they deduce the force term to be included in the Navier-Stokes equations, which they solve using a stream-function vorticity method. A limit of this approach is that solving the KZK equation for the propagation problem is very time-consuming since this transient nonlinear equation must be solved on every point of the mesh used for the Navier-Stokes solver, though the significance of the acoustic nonlinearity influence on the generated velocity field remains questionable. At the same time, they investigate the acoustic streaming velocity field using the LDA technique, which allows a local measurement of the velocity. They obtain detailed transverse velocity profiles, but have a poor spatial resolution in their longitudinal velocity profiles, with only six data-points for the 27cm long fluid domain. The comparison between the numerical and experimental transverse velocity profiles supports the reliability of their numerical model. However, the numerically obtained longitudinal velocity profiles exhibit an undulating shape which cannot be confirmed experimentally due to the lack of spatial resolution. Our contention is that such a shape can probably be correlated to the complex longitudinal profile of the acoustic beam in the near field. Such correlation between velocity and acoustic intensity is only discussed in Kamakura *et al.* (1996) for transverse profiles taken close to the Fresnel length. They underscore the fact that the velocity profile shape only transiently looks similar to the acoustic intensity profile shape, *i.e.* featuring one central peak and two secondary local maxima; on the contrary, the steady state velocity profile features only one, smooth, maximum on the centerline. For the other velocity profiles taken closer to the source, unfortunately, no explicit velocity to acoustic intensity comparison is given.

In the present paper the geometry is close to that of Kamakura *et al.* (1996), although the diameter and the frequency of the source are different. The former study [16] indeed considered a higher frequency, f, but a smaller source diameter, d_s, so that the near-field size, *i.e.* the Fresnel length, $L_f = d_s^2/(4\lambda)$, is similar in both studies. An objective of our study is to experimentally validate the force model given by equation (1) in the near field region where the legitimacy of the plane wave assumption is questionable. For that, we rely on space resolved velocity profiles obtained by the PIV technique. Another objective is to show that a numerical model based on linear acoustic propagation is able to accurately simulate this type of flow in the investigated parameters range. A final objective is to confirm that steady state transverse velocity profiles can show strong similarities with intensity profiles, for instance concerning the number of local maxima.

2 Experimental set up

The experiments are performed within an aquarium filled with water. The sound source is a 2MHz ultrasonic circular plane transducer from $Imasonic^{TM}$, with a diameter of 29mm. As depicted in figure 1, the domain of investigation is a rectangular cavity of inner dimensions $265 \times 180 \times 160$mm (length × width × height) with a top free surface. It is delimited by two 10mm thick *Apflex F28* absorbing walls, hatched on the figure, from $PrecisionAcoustic^{TM}$. The end wall is placed at $x_L = 275$mm from the transducer, *i.e.* at the end of the acoustic near field, in order to prevent standing waves to form in the investigated domain. The other wall, referred to as the intermediate tile and placed close to the transducer, has been drilled with a 63mm hole. The diameter of the hole has been chosen as about twice the transducer diameter in order to avoid modifying the acoustic pressure field. The hole was covered with a thermoretractable plastic film to let the sound enter in the investigation area but, at the same time, provide a rigid wall condition for the generated flow. The distance between the transducer surface and the plastic film is $x_0 = 10$mm. This set-up has already been described in our previous experimental paper [13]; it is also presented in more details in Moudjed's PhD thesis [17].

A needle hydrophone from $PrecisionAcoustics^{TM}$, held on a 3D motorized system, is used to map the acoustic field. A $Lavision^{TM}$ Particle Image Velocimetry (PIV) system is used to measure velocity field. Image acquisition is made with a 12 bit $PCO\ Sensicam^{TM}$ CCD camera with a resolution of 1280×1024 pixels. In our measurements, we use a double frame mode with a frequency of 4Hz; 6000 double frames are acquired as soon as the transducer is switched on, so that acquisition lasts about 25min. The time between the frames of each image pair is chosen to be 120, 90 and 50ms for **transducer** electric powers of respectively 2, 4 and 8W, in order to optimize the apparent displacement of the seeding particles. The de-ionised water used was seeded with 5μm Polyamid Seeding Particles (PSP) of density 1030kg.m^{-3} from $Dantec^{TM}$. The water temperature was measured to be 23°C. **Very precise positioning and thickness adjustment of the laser sheet are required since velocity gradients are strong. A 3D motorized displacement ensures the precise positioning and a homemade optical system is used to generate a laser sheet of less than 1mm in thickness.**

PIV measurements were made in two 20cm long and 16cm wide areas of the xy horizontal middle plane with an overlap region, to ensure a sufficient spatial resolution while observing the whole region of interest. The first zone extends from $x = 10$mm, *i.e.* from the sound absorbing intermediate wall, to $x = 205$mm and the second zone extends from $x = 80$ to $x = 275$mm, *i.e.* to the downstream sound absorbing wall.

3 Numerical model

To simulate the flow, we consider a rectangular cavity with dimensions $265 \times 180 \times 160$mm (length × width × depth) filled with water. The top free surface is assumed to be plane with a free slip condition for the flow and all the other boundaries are considered as rigid with a no-slip condition. Laminar, 3D, incompressible computations are performed with the commercial software $StarCCM+^{TM}$, which solves the Navier-Stokes equations with an additional acoustic force term :

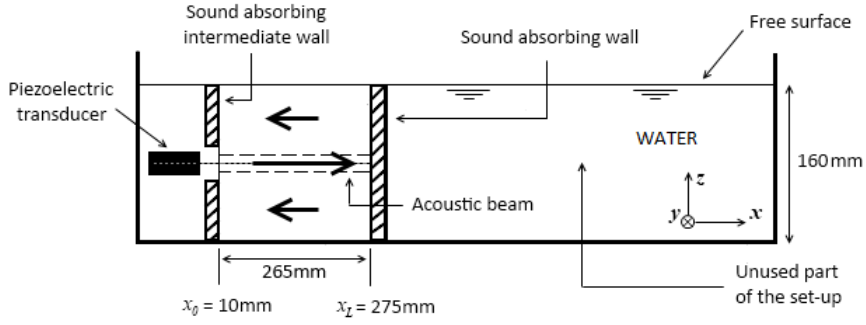$$\rho\frac{d\vec{u}_e}{dt} = -\overrightarrow{\text{grad}}p_e + \vec{f}_{ac} + \mu\Delta\vec{u}_e \ , \tag{2}$$

FIGURE 1 – Experimental set-up, view from the side. The origin of the Cartesian frame is set at the middle of the transducer plane surface : x-axis coincides with the propagation direction, y and z axis are respectively horizontal and vertical.

where $\vec{u}_e$ is the flow velocity (m.s^{-1}), p_e is the hydrodynamic pressure (Pa), $\vec{f}_{ac}$ is the volumetric acoustic force (N.m^{-3}) defined by equation (1), ρ is the fluid density ($\rho = 1000$kg.m^{-3}) and μ is the dynamic viscosity ($\mu = 10^{-3}$Pa.s). This equation was derived with a time scale separation method, which is detailed in a former paper [13].

Cubic cells are used to mesh the fluid domain. A cylindrical zone, where the mesh is refined, is created around the location of the acoustic beam. A mesh convergence study lead us to choose cells with a 0.5mm side in the central cylindrical zone and with a 2mm side in the rest of the fluid domain [17] ; the total number of cells is then 3.82 million. The acoustic force is computed with *Matlab*™ at each cell center using equation (1). The calculation of the acoustic intensity field, which appears in equation (1), is based on the Huygens-Fresnel assumption. The plane circular acoustic source is discretized with 200×200 elements. Each element has a surface $\Delta S = \sigma \Delta \sigma \Delta \alpha$, where σ and α are the polar coordinates (in the yz plane) of the element center, and is considered as a secondary source emitting a spherical wave. The resulting acoustic intensity field is calculated at any location (x, y, z) in the fluid domain by adding each secondary source contribution. It is then expressed using Rayleigh's integral as :

$$I_{ac} = \frac{I_{ac\,max}}{4\lambda^2} \left| \sum_{n=1}^{N} \sum_{m=1}^{M} \frac{e^{-i\frac{2\pi}{\lambda}\sqrt{x^2+y^2+z^2+\sigma_n^2-2\sigma_n y \cos(\alpha_m)-2\sigma_n z \sin(\alpha_m)}}}{\sqrt{x^2+y^2+z^2+\sigma_n^2-2\sigma_n y \cos(\alpha_m)-2\sigma_n z \sin(\alpha_m)}} \sigma_n \Delta\sigma\Delta\alpha \right|^2 , \qquad (3)$$

where $I_{ac\,max}$ is the maximal acoustic intensity, which is reached at the Fresnel length. The source diameter, d_s, is implicitly present in equation (3) since it defines the maximum value of σ_n. The acoustic intensity field given by equation (3) can be adjusted to the I_{ac} measurements by means of a least mean squares method, with two adjustable parameters, $I_{ac\,max}$ and d_s. Though we consider the hydrophone measurements to be reliable in a relative sense to obtain the acoustic pressure spatial variations in an experimental run, they are, however, very imprecise concerning acoustic pressure values in an absolute sense ; the confidence interval given by *PrecisionAcoustics*™, the supplier of this gauge, is indeed $\pm13\%$ on the acoustic pressure, *i.e.* $\pm26\%$ on the acoustic intensity. Another issue is that the determination of $I_{ac\,max}$ from the applied electric power P is also not possible as we know neither the electric losses in our system nor the efficiency of the transducer. As a consequence, we consider that reliable values of $I_{ac\,max}$ cannot be thus deduced from these measurements. We then rather chose to make an adjustment between the longitudinal velocity profiles obtained in the experiments and simulations by tuning the acoustic force level used in the simulations. This allows thus to get rid of the uncertainties on the hydrophone measurements, the efficiency and losses of the acoustic source, but also of those on the acoustic attenuation coefficient, already discussed in our former paper [13]. This acoustic force level is characterized by the maximum value of the force, $f_{ac\,max}$, reached on the beam

axis at the Fresnel length. Rough adjustments lead to the values $f_{ac\,max} = 0.725$, 1.5 and 2.9N.m^{-3} to be used in our simulations to compare with the experiments at $P = 2$, 4 and 8W, respectively. We can note the good proportionality between the chosen $f_{ac\,max}$ values and the applied electric power.

On the contrary, an adjustment based on the normalized fields was able to evaluate d_s at 28.5mm, a value which is very close to the transducer nominal diameter (namely 29mm), indicating that the structures of the measured acoustic field and the theoretical I_{ac} field are very close; it is confirmed when comparing normalized transverse acoustic intensity profiles (see [17] for more details). With this value of d_s, the Fresnel length is $L_f = d_s^2/(4\lambda) = 274$mm.

The coupled Navier-Stokes solver uses a second order upwind implicit finite volume scheme. A steady solver is used for $f_{ac\,max} = 0.725$ and 1.5N.m^{-3}; for $f_{ac\,max} = 2.9$N.m^{-3}, a second order implicit time scheme is used. In this last case, the results presented hereunder correspond to the steady regime reached with this unsteady solver.

Wavefronts of acoustic waves are depicted in figure 2 through isovalues of phase, calculated from equation (3). They are plotted around $x = 100$mm (fig. 2a) and $x = 150$mm (fig. 2b) in the near field and around $x = 274$mm (fig. 2c) and $x = 549$mm (fig. 2d) in the far field. As the wave length is very short ($\lambda = 0.74$mm), phase isocontours are represented in a very thin area of 2mm lenght and on a long transverse length, namely more than two diameters. Thus, several wave lengths are clearly visible on a transverse length greater than the source diameter. It can be noted that both, in the near field and in the far field, isovalues are not rigourously straight. However, in the central part between $y = +20$mm and $y = $-20mm, the gap on the longitudinal scale x for a same isovalue between $y = \pm 20$mm and the center is very short compare to the source diameter, so that acoustic wave can be considered as plane in this part. Outside of this part, namely above $y = +20$mm and below $y = $-20mm, isovalue are bended but straighten along the far field with the diffraction. To conclude, plane wave assumption use to established equations (1) and (3) is thus legitimated in the main area of the acoustic beam and the hydrodynamic jet.

4   Comparison of experimental and numerical results

The experimental velocity fields measured for $P = 4$W and the corresponding numerical velocity fields obtained for $f_{ac\,max} = 1.5$N.m^{-3} are plotted in the xy horizontal plane in figures 3a and 3b, respectively. A good agreement on the global flow structure can first be noted between the experimental measurements and the numerical calculations. As expected, the flow is characterized by a central jet with a very slow backflow on the sides of the fluid domain. A comparison with the velocity fields corresponding to the two other acoustic power values shows that the flow structure does not depend on the acoustic power in the investigated range [17]. A close look at the transverse velocity profiles in this vector plot allows to see that they exhibit one or several local maxima, depending on the considered abscissa, as expected from Kamakura *et al.* (1996).

Figure 4a shows the variations of the longitudinal velocity along the acoustic beam axis at $P = 2$, 4 and 8W. As already mentioned, each profile has been measured in two separate PIV runs; between these two runs, the camera and the illuminating laser sheet had to be moved along the
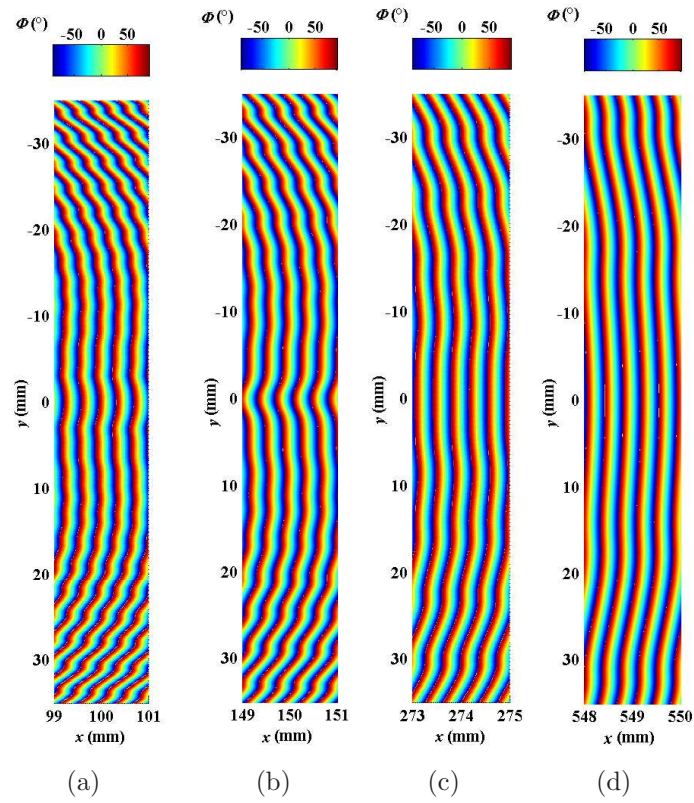
FIGURE 2 – Plot of phase isocontour in the near field around (a) $x = 100$mm and (b) $x = 150$mm, and in the far field around (c) $x = 274$mm $(= L_f)$ and (d) $x = 549$mm $(= 2L_f)$.
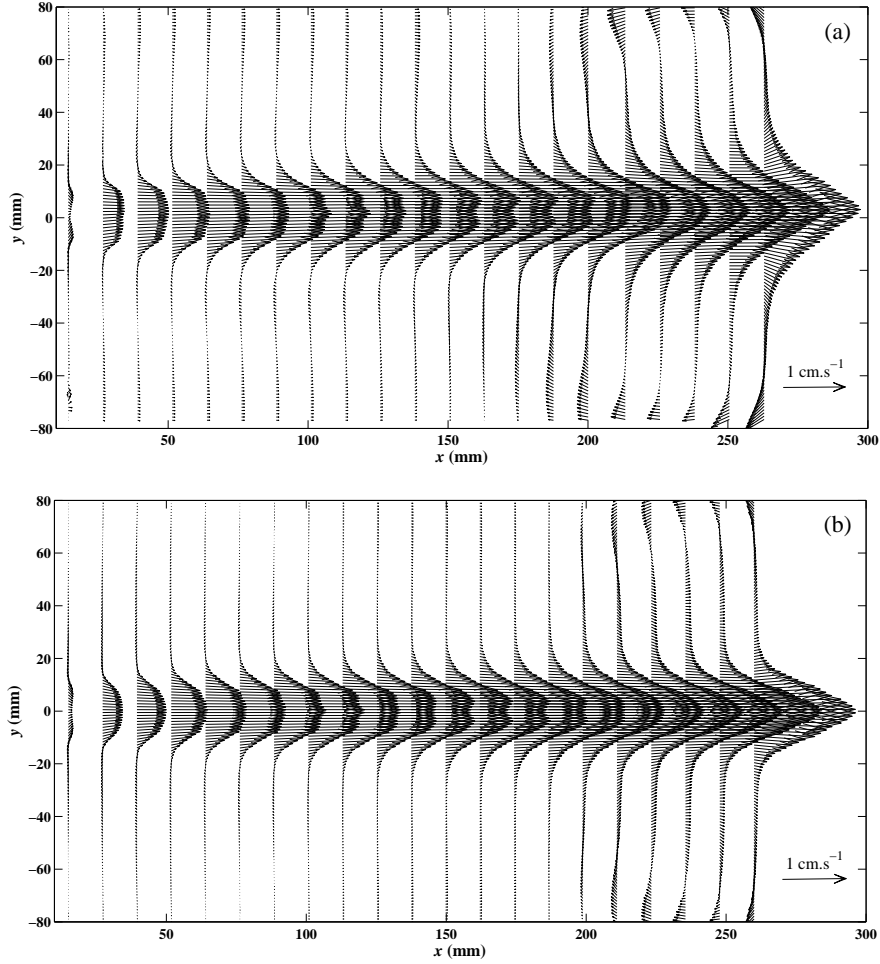
FIGURE 3 – Velocity vector maps in the xy horizontal plane including the acoustic beam axis. (a) Experimental measurements with the PIV technique for $P = 4W$, (b) Numerical computations for $f_{ac\,max} = 1.5 \text{N.m}^{-3}$. The velocity fields for the two other considered values of P can be found in Moudjed's PhD thesis [17].

aquarium with the risk of modifying the alignment of the laser sheet with the acoustic beam axis. In spite of this, there is a good linking between the two parts of these profiles, as can be seen in figure 4a. The profiles obtained numerically are also plotted with red dashed lines and a good agreement with the experimental profiles is observed. The axial velocity increases throughout the major part of the cavity and eventually drops suddenly to zero, as a consequence of the no slip condition at the end-wall. The initial curvature of the profiles, at small abscissa, is unexpectedly positive on a distance of a few millimeters. A wavering of the velocity profiles is also observed in a large part of the increasing portion. Note finally that electric powers of 2, 4 and 8W yield maximum velocities of 1, 1.5 and 2.1cm.s^{-1}, respectively.

The numerical velocity profiles are then normalized and plotted with the normalized acoustic intensity profile in figure 4b. This acoustic intensity profile along the acoustic beam axis is an exact analytic solution of Rayleigh's integral [18]. Note also that, in figure 4b, the abscissa is scaled with the Fresnel length. The local over-velocities and local under-velocities clearly correspond to the position of the acoustic intensity extrema. From the location of the last minimum of I_{ac} to the Fresnel length, the acoustic intensity increases; the axial velocity does as well, except close to the end-wall. Note here again that the velocity profile shapes are very similar for the three considered values of electric power.

Figure 5 provides the normalized transverse velocity profiles obtained experimentally at $x =$ 50, 100, 150 and 200mm from the transducer surface for the three considered powers. The normalized experimental acoustic intensity profiles at the same locations are also plotted as dashed lines, together with the normalized numerical velocity profiles obtained for $f_{ac\,max} = 1.5$N.m^{-3} plotted as solid lines. It can first be observed that, regardless of the acoustic power, the experimental velocity profile shapes are very similar, except in the low velocity backflow region. Such shapes are also reproduced by the normalized numerical velocity profiles. Moreover, a correlation can here again be noted between the shape of the acoustic intensity profiles and the shape of the velocity profiles. For instance, at $x =$ 100mm, the maximum velocity corresponds to the acoustic intensity central peak. At $x = 150$mm, the two local velocity maximums correspond to the two acoustic intensity peaks. Closer to the Fresnel length, as for $x = 200$mm, acoustic and velocity profiles become smoother and closer in shape to those expected in the acoustic far field [13], whereas at a small distance from the transducer, as for x = 50mm, the velocity profile does not follow the rapid spatial variations in acoustic intensity. Thus, though the correlation in shape between velocity profiles and acoustic intensity profiles is not perfect, we observe steady-state velocity profiles featuring several local maxima corresponding to local acoustic intensity maxima. Such observation was only done by Kamakura *et al.* (1996) for transient velocity profiles.

Note that we only focus here on the jet part of the flow. The backflow is indeed very slow : as a consequence of mass conservation, for a velocity of 2cm.s^{-1} in the central part of 3cm in diameter, a fluid particle in the backflow region will take more than eight minutes to cross the cavity length. A precise quantitative characterization of the flow in such a low velocity region would need a specific experimental treatment, which is out of scope of the present paper.

5   Scale analysis

As shown in our former paper [13], the balance between inertia effects and the acoustic force in the case of a free acoustic streaming jet can be written, on the beam
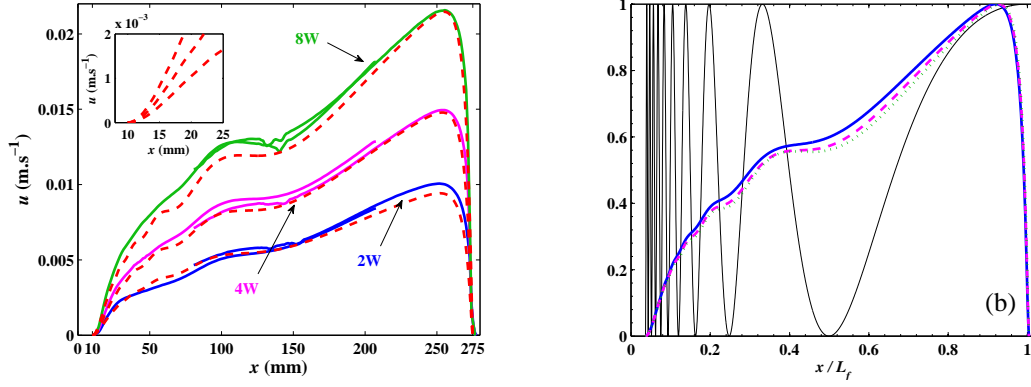
FIGURE 4 – Longitudinal profiles along the acoustic beam axis of (a) the experimental axial velocity for $P = 2$W (blue solid lines), 4W (pink solid lines) and 8W (green solid lines) ; the profiles obtained by the corresponding numerical calculations are also plotted as red dashed lines for $f_{ac\,max} = 0.725$, 1.5 and 2.9N.m^{-3}. These last one are normalized in (b) with blue solid lines, pink dashed lines and green dotted lines, restectively ; normalized acoustic intensity is plotted as black line (analytical expression after Blackstock (2000).

axis, as :

$$\rho\frac{\partial u_e^2}{\partial x} \sim f_{ac} , \tag{4}$$

which leads to the following scaling law :

$$u_e \sim \sqrt{\frac{f_{ac\,max}}{\rho}x'} . \tag{5}$$

with $x' = x - x_0$, where x_0 stands for the abscissa of the upstream wall (fig. 1). This scaling law has already been observed experimentally in the acoustic far field [13], but it was expressed with the acoustic power P_{ac}.

     In figure 6, the velocities u_e calculated on the beam axis for the three values of $f_{ac\,max}$ are plotted as a function of the expression under the radical sign in equation (5). Simulations results in the near field obtained by Kamakura *et al.* (1996) are also plotted. Let us recall that Kamakura's experiment featured a source of different diameter and frequency, so that the plot of their data with ours is in itself a good test of the proposed scaling law ; in particular the attenuation coefficient in their experiment is expected to be 5.7 times larger. For each numerical velocity profile plotted in figure 6, a good agreement with the scaling law given by equation (5) can be observed in an intermediate range of the abscissa values. In fact, these ranges correspond for each profile to the major part of the cavity, where the square root behavior is valid. Of course the scaling is not valid near the end wall due to the zero velocity condition at the wall. The scaling is also not observed near the upstream wall in a region where the velocity profiles have an unexpected initial positive curvature. **In this region, which is typically 5 millimeters long in our experiments, the velocity can be expected to evolve as $(x - x_0)^2$ (fig. 4). To demonstrate it, a mass conservation was made in a thin transverse slice, close to the upstream wall, between the tangential inflow and the axial outflow as depicted in figure 7. The tangential velocity can be written as :**

$$v_e \sim V_{peak}\frac{x'\left(x' - 2\delta\right)}{\delta^2} , \tag{6}$$
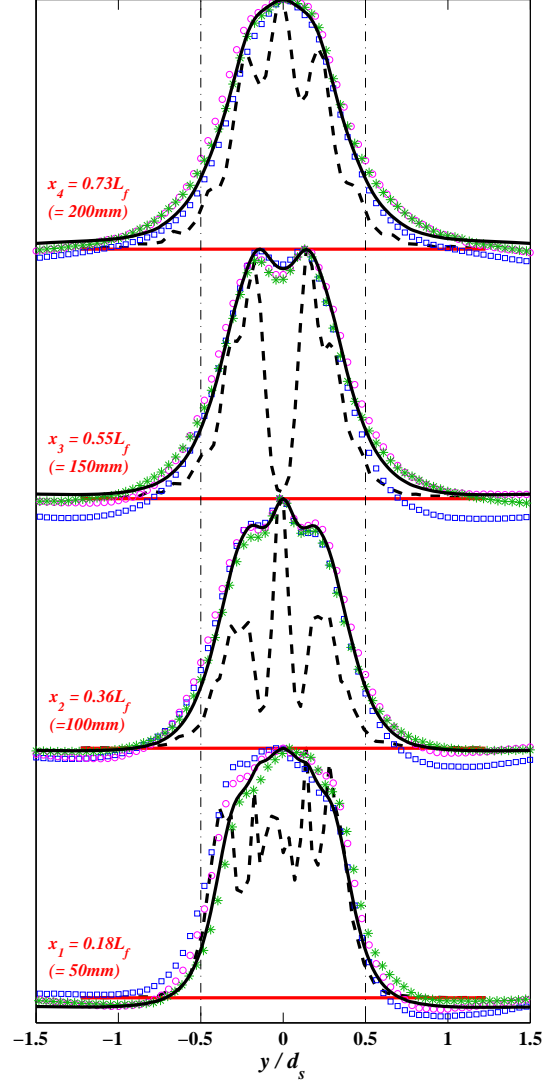
9

FIGURE 5 – Horizontal transverse profiles of the normalized experimental acoustic intensity (black dashed lines), the normalized experimental velocity at $P = 2W$ (blue open squares), $4W$ (pink open circles) and $8W$ (green stars), and the normalized numerical velocity calculated with $f_{ac\,max} = 1.5N.m^{-3}$ (black solid lines). These profiles are plotted at a distance $x = 50$, 100, 150 and $200mm$ from the transducer. The black dashed-dotted vertical lines indicate the acoustic source diameter. Note that these plots are focused on the jet region, so that the location of the lateral walls ($|y|/d_s \approx 3.2$) is not represented.

where δ represents the length of the control volume, namely the length over which the velocity longitudinal profile has a positive curvature ($\delta \approx 5mm$), and V_{peak}, the transverse velocity at $x = \delta$ and $y = d_s/2$ as depicted in figure 7. By mass conservation, the axial velocity can thus be expressed as :

$$u_e \sim \frac{d_s}{\delta^2 R_l^2} \left(\frac{x'^3}{3} - \delta x'^2 \right) V_{peak} \, , \tag{7}$$

with R_l the width of the the control volume : from the beam axis at $y = 0$ to the distance $y = R_l$, the axial velocity is constant so that the flow rate is simply written as $\pi R_l^2 u_e$. The distance R_l is typically 12mm. To get the scaling law expected, we have to remove $x^3/3$ from equation 7. This term can be neglected compared to $\delta x'^2$ for small values of x', Thus, equation 7 becomes :

$$u_e \sim \frac{d_s x^2}{\delta R_l^2} V_{peak} \, . \tag{8}$$

This last equation is plotted with black dashed line in figure 6.
Finally, an interesting point is to evaluate the limit distance x_{lim} between the two scaling laws, namely equation 5 and equation 8. This limit distance is found to be :

$$x_{lim} \sim \frac{R_l^4 \delta^2}{d_s^2 \rho} \frac{f_{acmax}}{V_{peak}^2} \, . \tag{9}$$

Numerical application drive to $x_{lim} \approx 11mm$, for $f_{ac\,max} = 0.725 \text{N.m}^{-3}$, which is about twice time higher than the expected value of 5mm. Firstly, in figure 6, intersection between the dashed line with a slope of 2 and the solid line with a slope of 1/2 corresponds not to a fixed value but more to the bended region which link points of the two regions. Thus there is a transitionnal area where the two scaling law are not suitable, so that the value of 11mm is in an interval which begins at the end of the scaling law of equation 8 and ended at the beginning of the square root scaling law of equation 5.

6   Conclusion and acknowledgements

The objective of the present work was a numerical and experimental investigation of the acoustic streaming flow in the near field of a plane ultrasonic transducer in water. To the best of our knowledge, our study is in particular the first to give spatially resolved experimental velocity profiles along the acoustic beam axis. A good agreement between the experimental measurements and the numerical results for the velocity field is obtained. Despite the complex structure of the acoustic near field featuring spatial variations at very small scales, the plane wave approach leading to the expression (1) for the acoustic force can thus be taken as valid in this area **and wavefronts plot in figure 2 supports this assum**. A linear acoustic propagation model is found to be suitable to compute the acoustic field and deduce the acoustic streaming force in the investigated range of parameters. Our acoustic propagation model is thus far simpler and lighter than the KZK model used by Kamakura *et al.* (1996). With a smaller computational time, it leads to results of the same quality concerning the correspondence between simulated flows and experiments. The strong correlation between the acoustic field shape and the flow structure is confirmed : the wavering observed on the longitudinal profiles of the velocity is linked to the variations in acoustic intensity on the beam axis, and the complex shape of the transverse velocity profiles is directly linked to acoustic intensity transverse variations. In particular, we observe for the first time steady-state transverse velocity profiles featuring several
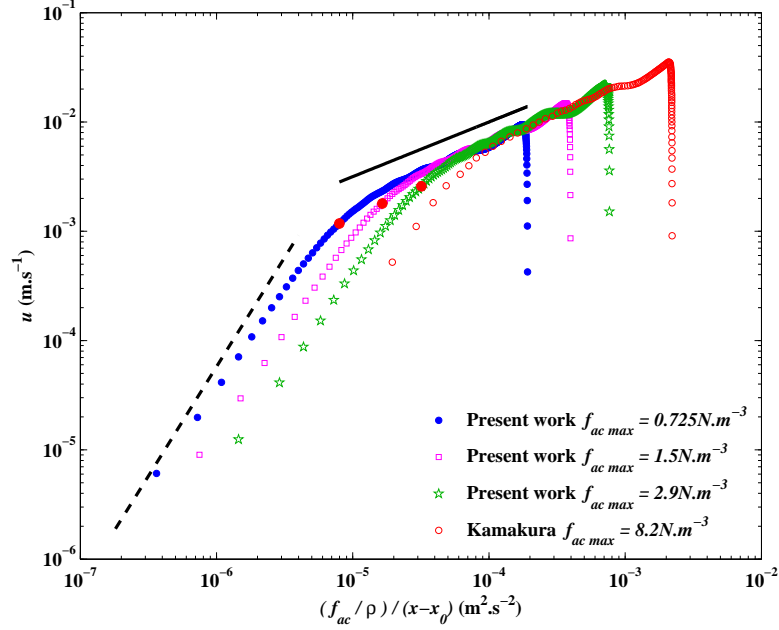
FIGURE 6 – Velocities calculated in the present work for the maximum values of the acoustic force $f_{ac\,max}$ = 0.725, 1.5 and 2.9N.m^{-3} and numerical velocities taken from Kamakura *et al.* (1996) are plotted as a function of the expression appearing under the radical sign in equation (5). **The black solid line corresponds to the right hand side under the radical sign in equation (5), so that the slope is 1/2 in the log-log plot. The black dashed line correspond to the right hand side in equation 8, adjusted with a coefficient, so that the slope is 2 in the log-log plot. Red filled point represents the value of x_{lim}, from equation 9, for $f_{ac\,max}$ = 0.725N.m^{-3}.**
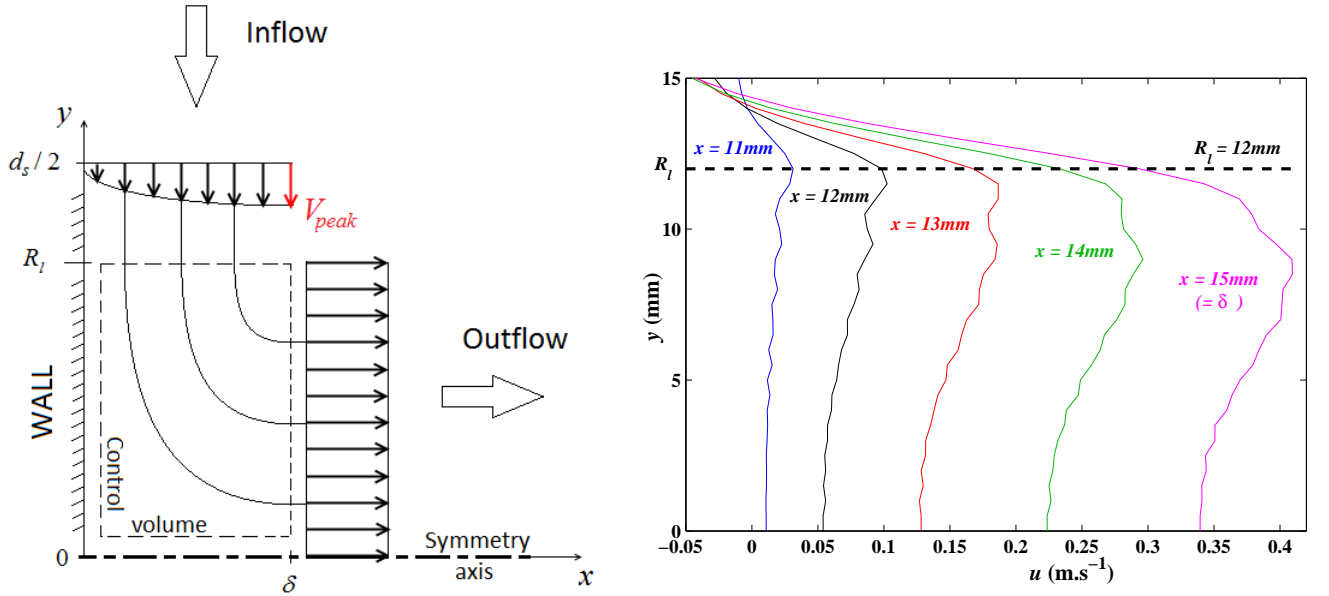

FIGURE 7 – **Two-dimensional view of the region close to the upstream wall. Mass conservation is performed in a volume control between the inflow (Poiseuille flow) and the outflow (parallel flow). Streamlines are represented with black lines.**

local extrema in correlation with those of the acoustic intensity profiles. Finally, our formerly derived scaling law for the velocity in the accelerating part of the jet is confirmed in the present configuration : the velocity increases as $(P_{ac}(x - x_0))^{1/2}$ over a major part of the cavity.

Références

[1] M. Faraday. On a peculiar class of acoustical figures ; and on certain forms assumed by groups of particules upon vibrating elastic surfaces. *Phil. Trans. R. Soc. Lond.*, pages 299–340, 1831.

[2] C. M. Poindexter, P. J. Rusello, and E. A. Variano. Acoustic Doppler velocimeter-induced acoustic streaming and its implications for measurement. *Exp Fluids*, 50(5) :1429–1442, 2011.

[3] A. Pothérat, F. Rubiconi, Y. Charles, and V. Dousset. Direct and inverse pumping in flows with homogeneous and non-homogeneous swirl. *Eur. Phys. J. E*, 36(8), 2013.

[4] L. Clarke, A. Edwards, and K. Pollard. Acoustic streaming in ovarian cysts. *JUM*, 24(5) :617–621, 2005.

[5] X. Shi, R. W. Martin, S. Vaezy, and L. A. Crum. Quantitative investigation of acoustic streaming in blood. *J. Acoust. Soc. Am.*, 111(2) :1110–1121, 2002.

[6] M. C. Charrier-Mojtabi, A. Fontaine, and A. Mojtabi. Influence of acoustic streaming on thermo-diffusion in a binary mixture under microgravity. *Int. J. Heat Mass Transf.*, 55(2122) :5992–5999, 2012.

[7] V. Frenkel, R. Gurka, A. Liberzon, U. Shavit, and E. Kimmel. Preliminary investigations of ultrasound induced acoustic streaming using particle image velocimetry. *Ultrasonics*, 39(3) :153–156, 2001.

[8] H. Ben Hadid, W. Dridi, V. Botton, B. Moudjed, and D. Henry. Instabilities in the Rayleigh-Bénard-Eckart problem. *Phys. Rev. E*, 86(1) :016312, 2012.

[9] W. Dridi, D. Henry, and H. Ben Hadid. Influence of acoustic streaming on the stability of a laterally heated three-dimensional cavity. *Phys. Rev. E*, 77(4) :046311, 2008.

[10] W. Dridi, D. Henry, and H. Ben Hadid. Influence of acoustic streaming on the stability of melt flows in horizontal Bridgman configurations. *J. Cryst. Growth*, 310(79) :1546–1551, 2008.

[11] M. C. Schenker, M. J. B. M. Pourquie, D. G. Eskin, and B. J. Boersma. PIV quantification of the flow induced by an ultrasonic horn and numerical modeling of the flow and related processing times. *Ultrasonics Sonochemistry*, 20(1) :502–509, 2013.

[12] Wesley L. Nyborg. *Acoustic streaming.* 1998.

[13] V. Botton, B. Moudjed, D. Henry, H. Ben Hadid, and J. P. Garandet. Scaling and dimensional analysis of acoustic streaming jets. *Submitted to Physics of Fluids*, 2014.

[14] S. I. Aanonsen, T. Barkve, J. N. Tjotta, and S. Tjotta. Distortion and harmonic generation in the nearfield of a finite amplitude sound beam. *J. Acoust Soc. Am.*, 75(3) :749–768, 1984.

[15] V. P. Kuznetsov. Equations of nonlinear acoustics. *Sov. Phys. Acoust.*, 16(4) :467–470, 1971.

[16] T. Kamakura, T. Sudo, K. Matsuda, and Y. Kumamoto. Time evolution of acoustic streaming from a planar ultrasound source. *J. Acoust. Soc. Am.*, 100(1) :132–138, 1996.

[17] B. Moudjed. *Caractérisation expérimentale et théorique des écoulements entraînés par ultrasons. Perspectives d'utilisation dans les procédés de solidification du Silicium Photovoltaïque.* PhD thesis, INSA de Lyon, 2013. In hal.archives-ouvertes.fr : hal-00958258.

[18] D. T. Blackstock. *Fundamentals of physical acoustics.* John Wiley & Sons, 2000.